Analysis of the Aesthetics of Semitransparent, Colorful, and Transparent Luminescent Solar Concentrators

Chenchen Yang,[1] Miles C. Barr,[2] and Richard R. Lunt[1,3,*]

[1] *Department of Chemical Engineering and Materials Science, Michigan State University, East Lansing, Michigan, 48824, USA*

[2] *Ubiquitous Energy, Inc., Redwood City, California 94063, USA*

[3] *Department of Physics and Astronomy, Michigan State University, East Lansing, Michigan, 48824, USA*

(Received 9 June 2021; revised 10 December 2021; accepted 15 February 2022; published 22 March 2022)

Luminescent solar concentrators (LSCs) are a key type of photovoltaic technology which features structural simplicity, angle independence, high defect tolerance and design flexibility. Since the concept of LSC was first introduced in the 1970s, LSCs have been envisioned to reduce the cost of deployed solar arrays, to enable seamless installation onto buildings with enhanced aesthetics, and more recently as glazing systems to improve overall on-site energy utilization efficiency. Widespread solar adoption requires LSCs to simultaneously achieve high photovoltaic performance and excellent aesthetic quality. With most research efforts focusing on efficiency improvements, the significance of LSC aesthetics has been understated. In particular, escaped photoluminescence has the potential to strongly impact visual aesthetics in several different ways and has been particularly overlooked. In this work, we define and analyze key figures of merit for LSC aesthetics by incorporating the impact of photoluminescence. Additionally, a new metric analogous to haze, termed the "average visible luminescent haze," is defined to describe the visual impact of escaped photoluminescence on human perception. The main mechanisms of photoluminescence utilized in LSC design, including downshifting, upconversion and quantum cutting, are systematically assessed within this framework. In identifying these key aspects, this perspective can help guide future research in semitransparent, colorful, and transparent LSC designs.

DOI: 10.1103/PhysRevApplied.17.034054

I. INTRODUCTION

An effective strategy to enhance the potential of solar energy collection is to seamlessly integrate photovoltaic (PV) devices onto the surfaces of our built environment, converting them into power-generating sources. Such deployment simultaneously enables on-site renewable energy generation and reduces electricity loss in transmission and distribution. This approach also expands viable applications to the architectural envelope (rooftops, façades, and sidings), electric vehicles, greenhouses, and mobile electronics, *inter alia*. [1]. To adequately fulfill the promise of these potential PV adoption opportunities, comprehensive understanding beyond photovoltaic performance is required of additional factors such as scalability, reliability, affordability, and, most importantly, aesthetic quality [2]. Luminescent solar concentrators (LSCs) were introduced as a cost-effective alternative to conventional solar cells. They continue to show great promise in building-integrated photovoltaics and other relevant applications [3,4].

The working principle of LSCs is shown in Fig. 1. Luminophores embedded in a transparent LSC waveguide harvest incident solar irradiance and reemit at different wavelengths in all directions [4,5]. The reemitted photons are predominantly trapped within the waveguide and directed towards the edges by total internal reflection, and then converted into electricity by attached PV cells. Since the flux is optically shifted to the edge-mounted PVs, the whole solar collection area is free of electrode patterning and busbars, significantly simplifying the device architecture. In the past decade, rapid development in nanostructured and excitonic materials has provided various luminophore species including quantum dots [6–14], nanoclusters [15–17], rare-earth ion complexes [18,19], and organic dyes [20–23], offering greater versatility and design freedom.

Much of the recent LSC research has been aimed at improving the performance and scalability of LSCs by improving the photoluminescence quantum yield (QY) [20,22,23], waveguide optics [24,25], solar spectral harvesting [6,8,17,26,27], surface losses [9,28], voltage losses [29–31], and reabsorption loss [6,10–14,16,19,32–34]. However, many of the factors that impact aesthetics are often overlooked despite these factors being the most

*rlunt@msu.edu

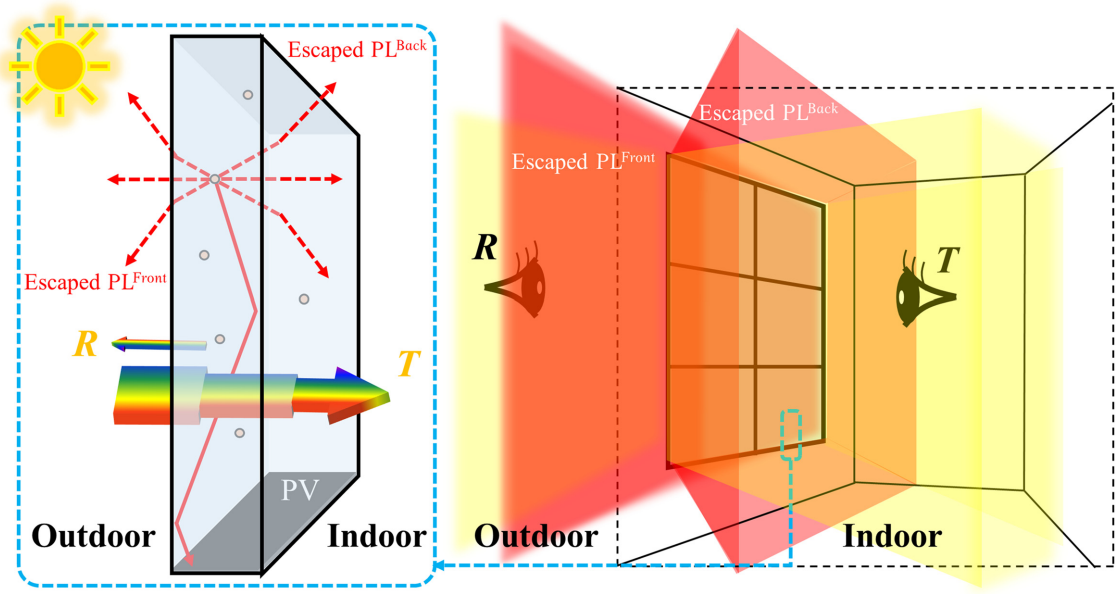

FIG. 1. Schematic showing the impact of escaped photoluminescence on the aesthetics of luminescent solar concentrator (LSC) systems. The incident sunlight beam is transmitted and reflected only in the normal direction (in light yellow), whereas the untrapped photoluminescence escapes from both waveguide surfaces in all directions (in red) which creates a "glowing" effect to observers on both sides. Therefore, the transmitted solar spectrum combined with the escaped photoluminescence spectrum [AM $1.5G(\lambda)\cdot T(\lambda) + PL^{Back}(\lambda)$] determines the aesthetic parameters of the LSC on the transmitted side (i.e., indoor side), and the reflected solar spectrum combined with the escaped photoluminescence spectrum [AM $1.5G(\lambda)\cdot R(\lambda) + PL^{Front}(\lambda)$] determines the aesthetic parameters of the LSC on the reflected side (i.e., outdoor side).

critical to market adoptability for many applications. In this work, we develop a framework to understand the impact of aesthetics in LSC design based on absorptance, transmittance, reflectance, and photoluminescence. We first identify the key figures of merit for aesthetic quality of transparent solar technologies. Then we incorporate photoluminescence to evaluate the corresponding impact on these key parameters. A new design parameter, the average visible luminescent haze, is defined to more precisely describe and quantify the visual perception induced by the escaped photoluminescence. Finally, we apply this framework to various LSC luminophores based on downshifting (DS), upconversion (UC), and quantum cutting (QC) mechanisms.

II. OPTICAL MODEL

A. Figures of merit and criteria for aesthetic quality

Transparent solar cells allow part or all of the visible photons to pass through the PV device to create visible transparency and harvest either part of the visible spectrum that is not transmitted or the invisible portion [ultraviolet (UV) and near-infrared (NIR)] photons to generate electric power. Additionally, LSCs with purposeful coloration can be enabled by tuning the corresponding absorption, transmission, reflection, and emission spectra, offering an approach to design the appearance and diversify the aesthetics of the applied surfaces [1,2,35,36]. Typically, the aesthetics of transparent photovoltaics (TPV) is quantitatively evaluated by using three key figures of merit: average visible transmittance ($AVT_{\perp}$), color rendering index (CRI) and CIELAB color coordinates (a^*, b^*) [1,24,37]. The $AVT_{\perp}$ is used to evaluate the overall visible transparency (weighted by the photopic response) of a given TPV device and is widely utilized in the window industry. CRI and (a^*, b^*) can be utilized to quantify the rendered color fidelity and indicate the relative color of the light transmitted or reflected by the device as test light source with respect to a reference illumination source, and both are utilized in the lighting and window industries [24,37,38]. Color purity (i.e., color saturation) is used to quantify the degree of a tinted color on the CIE 1931 (i.e., CIEXYZ) chromaticity diagram, which quantitatively evaluates the degree of closeness of the tinted color compared to the dominant monochromatic color. In the CIE 1931 chromaticity diagram, monochromatic colors are located along the perimeter of the chromatic diagram, which is also referred to as the spectral locus. The (x, y) coordinates of air-mass 1.5 global (AM 1.5G) (0.332, 0.344), CIE standard illuminated D65 (0.313, 0.329), and equal energy point (1/3, 1/3) are also included in the CIE 1931 plot: the corrected color temperature of the AM 1.5G and D65 are approximately 5513 K and 6504 K along the

proximity of Planckian locus, respectively, both very close to the equal energy point. AM 1.5G energy flux (in units of watts per square meter per nanometer) is the standard input power intensity widely adopted by solar industry, whereas D65 is a unitless spectrum profile based on the blackbody radiation curve at approximately 6500 K that is commonly used as the standard illuminant to represent daylight illumination in both lighting and window industries. As TPV technologies develop, photovoltaic performance and aesthetic quality become equally important for practical deployment, requiring a merger of the PV and CIE standards. In TPV deployment, these devices are illuminated by an incident solar spectrum that simultaneously dictates both the power conversion efficiency (PCE) and aesthetics. Therefore, it is only logical to apply one unified spectrum standard in units of power per area only for all measurements and both purposes [24,37,39]. In comparison, $AVT_{\perp}$s of various transmittance profiles are calculated based on both AM 1.5G and D65 spectra, the absolute discrepancies are generally below 1% unless the transmission is severely tinted. Nonetheless, we provide the optical properties based on D65 for reference (see Supplemental Material Note 1 and Note 4 for details [66]).

To design TPVs so as to simultaneously maximize the light harvesting (PCE) and optimize the corresponding visual appearance, it is necessary to define the proper visible spectral range by considering the three key aesthetic parameters. Since the AM 1.5G under 1 sun intensity (1000 W m^{-2}) has been widely adopted as the test standard for incident solar irradiation in PV characterization since the 1970s [37,40,41], we use AM 1.5G as the reference spectrum (reference illumination source) for the calculation of all the aesthetic parameters [i.e., AM 1.5G alone as the input test light source yields an $AVT_{\perp}$ of 100%, a CRI of 100 and the (a^*, b^*) at the origin (0, 0)]. Idealized step-function transmittance profiles with varying cutoffs are utilized to confirm the practical visible range (VIS) for TPVs. Previously, the visible range had been defined for the purposes of optimizing TPVs with minimal visual impact as 435–675 nm based on CRI > 95 only [5,17,23,24,37]. Here we consider and assess the color metrics of both CRI and (a^*, b^*) in depth. We first survey 50 of the top mass-market architectural low-E glass products (see Supplemental Material Note 2 for the statistics [66]) to determine the industry targets for the majority of transparent window products. From this analysis we find that CRI ≥ 85, and $-7 < a^* < 0$, $-3 < b^* < 7$ are key levels for widespread product deployment where the (a^*, b^*) become the key constraining factors over the CRI. As shown in Figs. 2(a) and 2(b), transmitting photons in the range of 430–675 nm with no light absorption provides a CRI of 96.70 and (a^*, b^*) = (−3.95, 6.37), adequately meeting these requirements while maximizing the solar harvesting in the invisible range. We note that the transmissive range is only slightly changed from 435 to 430 nm on the blue/UV side so that the corresponding b^* value slightly decreases from 9.17 to 6.37 and falls within the acceptable range. When the long-wavelength cutoff is

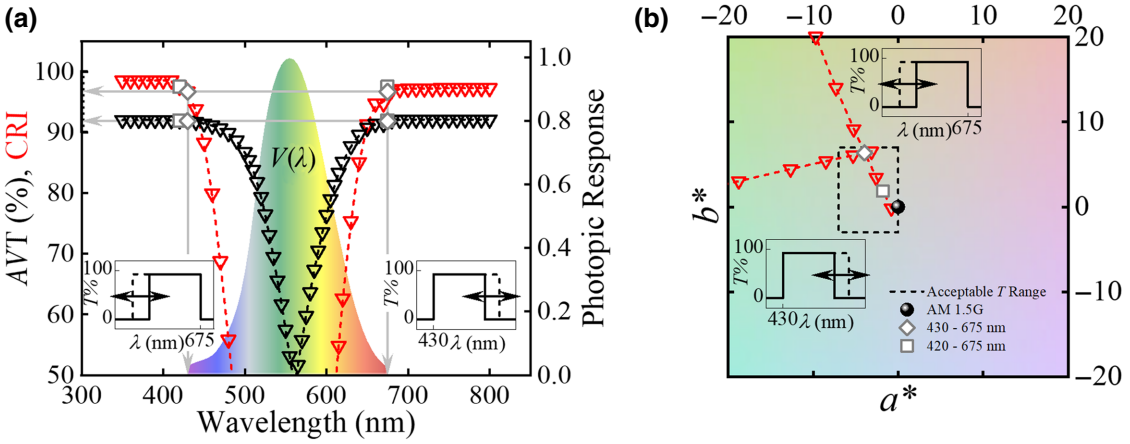

FIG. 2. (a) Color rendering index (CRI_T, red triangle) and average visible transmittance ($AVT_{\perp}$, black triangle) of the TPVs as a function of short and long idealized visible transmission wavelength cutoff shown in the insets. The photopic response [$V(\lambda)$] is also included as the background. The AM 1.5G solar spectrum is used as the reference light source, which results in a CRI_T value of 100. (b) CIELAB color coordinates $(a^*, b^*)_T$ as a function of short and long idealized visible transmission wavelength cutoff shown in the insets. The acceptable $(a^*, b^*)_T$ range based on mass-market architectural glass products is plotted as the dashed box, $-7 < a^* < 0$ and $-3 < b^* < 7$, and the reference spectrum AM 1.5G is at the origin (0, 0). With comprehensive consideration of both color metrics, the visible range is therefore defined as 430–675 nm, which results in CRI_T of 96.70 and (a^*, b^*) = (−3.95, 6.37) [indicated as gray diamonds in (a) and (b)], while a stricter definition of visible range, 420–675 nm, results in CRI_T of 97.51 and (a^*, b^*) = (−1.80, 1.87) [indicated as gray squares in (a) and (b)].

fixed at 675 nm, redshifting the short-wavelength cutoff from 430 nm quickly decreases CRI and rapidly increases b^* in the positive direction, resulting in perceptible yellow/orange tinting; similarly, with fixed short-wavelength cutoff at 430 nm, blueshifting the long-wavelength cutoff from 675 nm into the VIS also quickly decreases CRI, and rapidly decreases $a^* < 0$, resulting in blue tinting. Thus, any further reduction in this defined VIS range imparts substantial visual impact on the corresponding TPVs (see Supplemental Material Note 1 for tabulated data [66]). Additionally, we note that blueshifting the UV/VIS cutoff from 430 to 420 nm while maintaining the NIR cutoff at 675 nm results in $(a^*, b^*) = (-1.80, 1.87)$, moving much closer to the CIELAB origin with a slightly higher CRI of 97.5 for the highest aesthetic demands. Any absorption or reflection peak located within the defined VIS range of 430–675 nm, particularly near the photopic response [$V(\lambda)$] peak as shown in Fig. 2(a), results in significant colored tinting, which dramatically reduces $AVT_\perp$ and CRI values and moves (a^*, b^*) far from the origin.

B. Transparent applications

The aesthetics of an LSC or any TPV device can be observed from both the transmitted and reflected sides. Thus, the total transmitted or reflected spectrum determines the aesthetics of each side. Intuitively, the key figures of merit for aesthetic quality in the glass industry or conventional TPVs can be readily transferred to the evaluation of LSC aesthetics. However, the escaped photoluminescence can cause significant visual impact on the LSC aesthetics. For simple waveguides with isotropic emitters and typical index of refraction (say, 1.5), approximately 25.5% of the total emitted photoluminescence photon flux [$PL^{Total}(\lambda)$] escapes from the emission cone (θ_C) from both front/back of the LSC waveguide as illustrated in Fig. 1 [4,5]. The escaped photoluminescence [$PL^{Back}(\lambda)$ or $PL^{Front}(\lambda)$, approximately 12.75% of $PL^{Total}(\lambda)$ on each side] combined with the transmitted or reflected solar spectrum [AM 1.5G$(\lambda)\cdot T(\lambda)$ or AM 1.5G$(\lambda)\cdot R(\lambda)$] determines the total photon flux on each side. While anisotropic emitters (e.g., dichroic dyes) can reduce the escaped PL, they cannot completely eliminate escaped PL [42]. If the photoluminescence [PL(λ)] resides within the VIS range, then the escaped photoluminescence becomes visually prominent and appears as if it were a "colorful haze."

Based on the defined VIS range, the idealized step-function absorption profiles in the invisible spectral ranges are determined, and the same normalized emission profile is manually shifted to create photoluminescence as a function of wavelength [PL(λ) in blue, cyan, green, orange, red, and NIR] as shown in Fig. 3(a) [4,5]. We note PL(λ) is the photoluminescence spectral profile normalized by its peak value, which is used for schematic purposes, whereas $PL^{Total}(\lambda)$, $PL^{Front}(\lambda)$, and $PL^{Back}(\lambda)$ are the absolute photoluminescence photon fluxes, which share the same unit with AM 1.5G photon flux (approximate number of photons per square meter per nanometer per second) and therefore are directly used as input photon fluxes for the calculation of various color metrics. Varying degrees of visible absorption are included. To isolate the impact from the photoluminescence only, we fix any visible absorption profile to be flat across the entire VIS to create color-neutral transmission. Appendix A provides the detailed calculation of total absorptance [$A(\lambda)$], reflectance [$R(\lambda)$] and transmittance spectra [$T(\lambda)$]. The multiplication factor (m) is defined as the number of emitted photons per absorbed photon, and the total impact is then assessed based on DS ($m = 1$), UC ($m = 0.5$), and QC ($m = 2$) photoluminescence mechanisms described below, respectively.

For indoor aesthetics, it is assumed that the window is the primary light source during the day of a given room as shown in Fig. 1. Thus, the visible $PL^{Back}(\lambda)$ impacts the rendered color fidelity of the transmitted sunlight and creates luminescent haze. Such haze can be observed as if the window is "glowing" in the color of the photoluminescence. A similar effect, but of differing magnitude, is expected for the outdoor aesthetics from $PL^{Front}(\lambda)$ that will impact the exterior appearance of the building. To comprehensively assess the aesthetics of LSC devices, these PL spectra are used to correct the AM 1.5G$(\lambda)\cdot T(\lambda)$ and AM 1.5G$(\lambda)\cdot R(\lambda)$ input spectra (i.e., test light sources) to calculate the rendered color with respect to the standard AM 1.5G spectrum (i.e., reference illumination source) on each side. Modified color rendering indexes (CRI_T and CRI_R) and CIELAB color coordinates [$(a^*, b^*)_T$ and $(a^*, b^*)_R$] are used to quantify the rendered colors on each side. The detailed CRI and (a^*, b^*) calculation approaches have been described elsewhere with available spreadsheet calculators already provided [24,37]. We note that the calculation of $AVT_\perp$ remains the same, which is still reported as the integration of $T(\lambda)$ measured at normal incidence and weighted against the photopic response [$V(\lambda)$] of the human eye [37].

For window products, scattering (in the bulk or on the surfaces of the glass sheet due to microscopic imperfections or textures during fabrication process) can cause haze that reduces optical quality and the transmission of optical information. Scattering haze is defined as the ratio of the transmitted light that is diffuse to the total transmitted light (the sum of specular transmittance and diffusive transmittance) [43,44]. In the case of photoluminescence, we incorporate $V(\lambda)$ into the definition of a new parameter, the average visible luminescent haze ($AVLH_T$ and $AVLH_R$ for the transmitted and reflected sides, respectively, see Appendix B for detailed calculation), to quantify the glowing haze of escaped photoluminescence for human perception.

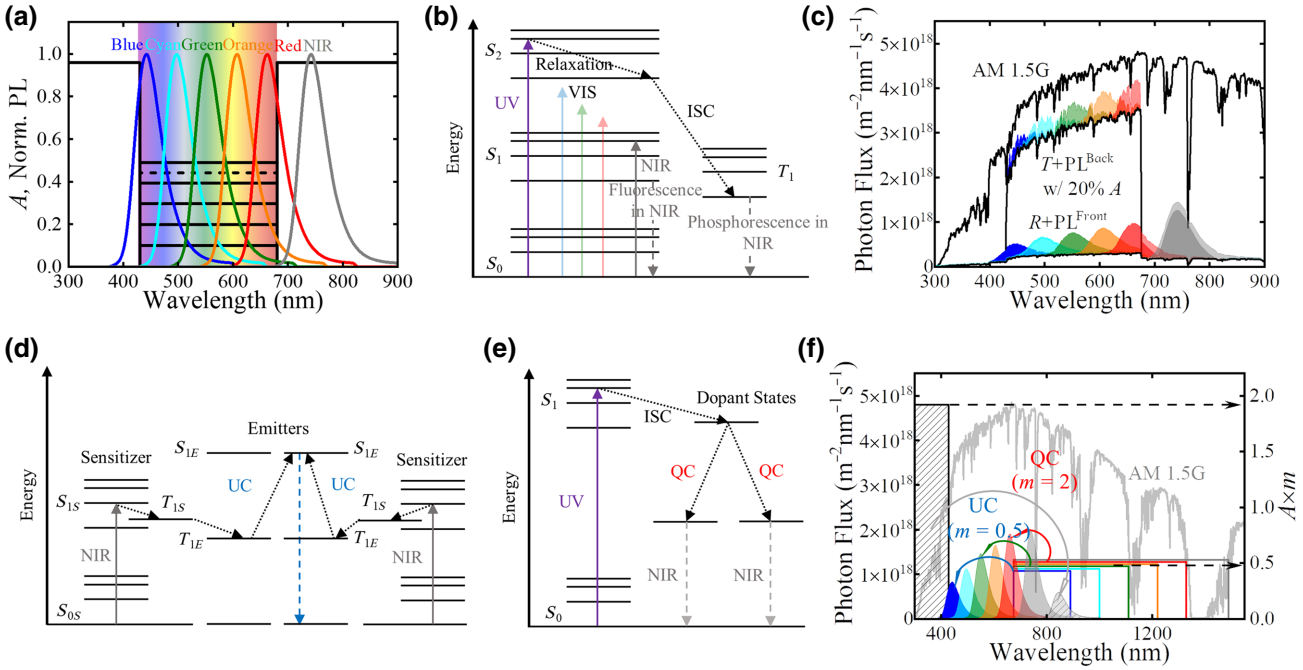

FIG. 3. (a) Schematic of idealized absorption and emission characteristics with step-function absorptance profiles with various degrees of visible contribution in the range 430–675 nm are drawn. The emission profile is manually shifted to create photoluminescence as a function of wavelength [PL(λ) in blue, cyan, green, orange, red and near-infrared (NIR)] in the optical model. (b) Jablonski energy diagram of the downshifting photoluminescence process. (c) An example to show the impact of escaped downshifting photoluminescence on the combined spectra on transmitted and reflected sides of an LSC system with 20% visible neutral single-pass absorptance (A_1). AM 1.5G photon flux is also included as background for comparison. Jablonski energy diagrams of (d) triplet-triplet annihilation upconversion (TTAUC) and (e) quantum cutting (QC) photoluminescence processes. (f) Idealized absorption and emission characteristics of spectral conversion approaches in LSC design: UV photons are quantum cut with emission in NIR; the usable IR range expands as the upconverted emission wavelength redshifts [PL(λ) manually shifted from blue to NIR]. Note that the product of the corresponding absolute absorptance heights (A) and the multiplication factors (m) is used as the right axis ($A \times m$) to signify these spectral conversion mechanisms.

C. Colorful applications

Comprehensive tunability in $A(\lambda)$, $T(\lambda)$, $R(\lambda)$, and PL(λ) can be effectively utilized and combined to purposefully create colored surfaces. In these cases, there color is imparted by transmission and reflection, as well as escaped PL. To demonstrate such designs, we further modify the idealized step-function absorption profiles in VIS and combine them with the VIS DS photoluminescence to purposefully create various transmitted and reflected colors (see Supplemental Material Note 5 for detail [66]). The same DS photoluminescence profiles shown in Fig. 3(a) are paired with these VIS absorption profiles, and the corresponding results of purposeful coloration are calculated with the same method as described in the previous section.

III. PHOTOLUMINESCENCE MECHANISMS

Downshifting, shown in Fig. 3(b), occurs when absorption of high-energy photons leads to photoluminescence with longer wavelengths via fluorescence or phosphorescence with a maximum QY of 100%. In this model, the QYs of all the DS processes are assumed to be 100%. To ensure energy conservation in all the $A(\lambda)$ and PL(λ) combinations, we only allow the absorbed photons with wavelengths shorter than the emission peak wavelengths to contribute to the DS photoluminescence, therefore, the total emitted energy (the sum of that escaped from the front and back of the waveguide and that trapped within the waveguide) is always lower than the total absorbed energy participating in the DS photoluminescence process. A typical example of how the DS $PL^{Back}(\lambda)$ and $PL^{Front}(\lambda)$ impact the total transmitted and reflected spectra is shown in Fig. 3(c). With 20% neutral VIS single-pass absorptance ($A_1 = 20\%$; see Appendix A for detail), the transmitted and reflected solar spectra [AM 1.5G(λ)·$T(\lambda)$ and AM 1.5G(λ)·$R(\lambda)$] are both determined, and the varying $PL^{Back}(\lambda)$ and $PL^{Front}(\lambda)$ as a function of emission wavelengths are then superimposed onto the transmitted and reflected solar spectra as the combined spectra AM 1.5G(λ)·$T(\lambda)$ + $PL^{Back}(\lambda)$ and AM 1.5G(λ)·$R(\lambda)$ + $PL^{Front}(\lambda)$ on the transmitted and reflected sides, respectively.

Another mechanism that can be conceptually utilized to enhance LSC performance is upconversion. UC takes

multiple low-energy photons below the energy band gap of the edge-mounted PV cells and converts them into a lower number of high-energy photons that can be converted to electricity in the PV cell. This mechanism effectively expands the solar spectral coverage achievable over the conventional DS process [26,45,46]. Currently, there are two main approaches to enable UC. In lanthanide-based upconverters, the absorbed photon energy is transferred from the codoped lanthanide sensitizers (e.g., Yb^{3+}) to emitters (e.g., Er^{3+}) with spectral overlap. However, this approach usually suffers from narrow solar spectrum coverage and inferior QYs, making it unsuitable for photovoltaic applications. Another UC approach is triplet-triplet annihilation upconversion (TTAUC). This mechanism tends to be more suitable for photovoltaic applications due to relatively higher optical absorption and QYs [47–49]. Figure 3(d) shows the energy transfer process of TTAUC. Sensitizer molecules are excited from ground state (S_{0S}) to excited state (S_{1S}) by absorbing low-energy photons. Then the excited sensitizer passes to a long-lived triplet state (T_{1S}) via intersystem crossing. Subsequently, the excited energy transfers from the sensitizer triplet state (T_{1S}) to the emitter triplet state (T_{1E}), and triplet-triplet annihilation (TTA) occurs between two emitters in close proximity to form a higher-energy singlet state (S_{1E}) that emits one upconverted high-energy photon [26]. By assuming ideal QYs of various UC processes of 50%, the idealized absorptance and emission profiles are shown in Fig. 3(f): the PL(λ) peaks (blue, cyan, green, orange, red, and NIR) shown in Fig. 3(a) are also used for UC emission, and a spectral range between 675 nm (VIS/NIR border) and up to twice the corresponding emission peak wavelengths (i.e., two low-energy photons are upconverted into one high-energy photon) can be potentially utilized for UC harvesting. In all these UC processes we confirm that the total absorbed NIR energy is higher than the total upconverted and emitted energy so that the energy conservation is always satisfied.

Quantum cutting is a process that effectively enhances DS. In this case, one high-energy photon is absorbed and split into multiple low-energy photons [50–54]. The energy diagram for QC process is shown in Fig. 3(e). Upon absorbing one high-energy photon, the excited singlet state (S_1) undergoes intersystem crossing to dopant states, where the QC process takes place and subsequently emits two low-energy photons. This spectral conversion approach enables effective utilization of high-energy UV photons in LSC applications, and the step-function absorptance and emission profiles for QC process with ideal QY of 200% is also plotted in Fig. 3(f). All the UV photons below 430 nm are split into multiple deeper NIR photons with a massive downshift across the VIS range. Notably, because the VIS/NIR cutoff is at 675 nm, quantum cutting NIR photons results in emission past 1350 nm, and it is very challenging to spectrally match such a deep IR emission with high efficiency edge-mounted PV cells. QC with emission in the visible range requires the absorbed UV light with photon energy over 3.7 eV (below 338 nm), and the corresponding high-energy UV photons flux (less than 0.4% of the total AM 1.5G photon flux) is negligible for electrical power generation. Therefore, these two cases are not considered in this work.

Similarly to the DS process, the combined spectra AM $1.5G(\lambda)\cdot T(\lambda) + PL^{Back}(\lambda)$ and AM $1.5G(\lambda)\cdot R(\lambda) + PL^{Front}(\lambda)$ resulting from the UC and QC mechanisms are also used to calculate the rendered color metrics affected by the escaped photoluminescence on each side. To date, DS is the most widely adopted photoluminescence mechanism in LSC design, with QYs near unity. Demonstrations of TTAUC [27,55,56] and QC mechanisms [50,52,53] in LSC systems have also been reported in literature, but TTAUC is still far from ideal due to its relatively low UC efficiency [46,48]. In contrast, near 200% QYs have been shown for QC mechanism despite less ideal absorption/emission profiles [50,51,53].

IV. RESULTS

A. Transparent applications

Figure 4 shows the impact of DS photoluminescence on neutral-colored LSC aesthetics as a function of various degrees of visible contribution. Architectural glass typically requires $AVT_{\perp}$s above 50%, which still allows design opportunities and flexibility to effectively harvest some visible photons for TPV power generation [1]. The $AVT_{\perp}$ linearly decreases as the VIS contribution (A_1) increases. However, as the visible absorption contribution increases, the overall intensities of $PL^{Back}(\lambda)$ and $PL^{Front}(\lambda)$ also increase, which can significantly affect the combined spectra and aesthetics on both sides (indoor and outdoor) of the LSCs.

In both the lighting and window industries, the color rendering can be categorized by the corresponding CRI ranges: typically, 95–100 is "excellent," 90–95 is "good," 85–90 is "acceptable," and below 85 is "poor" for neutral-colored requirements which are indicated with different shades of color in Figs. 4(a) and 4(d). As more incident photons are harvested and downshifted into the visible photoluminescence, the corresponding CRI_T and CRI_R values drop accordingly. On the transmitted side, the CRI_Ts degrade with all visible PL colors but still remain within or above the acceptable range as long as the visible contribution (A_1) is below 50%. On the reflected side, however, all the CRI_Rs immediately degrade to an unacceptable range even without any visible absorption contribution. We also see the impact of $PL^{Back}(\lambda)$ and $PL^{Front}(\lambda)$ on (a^*, b^*) in Figs. 4(b) and 4(e), respectively. The increasing VIS photon contribution can quickly move the (a^*, b^*) away from (0, 0) towards the corresponding colors of the visible photoluminescence, driving the corresponding color

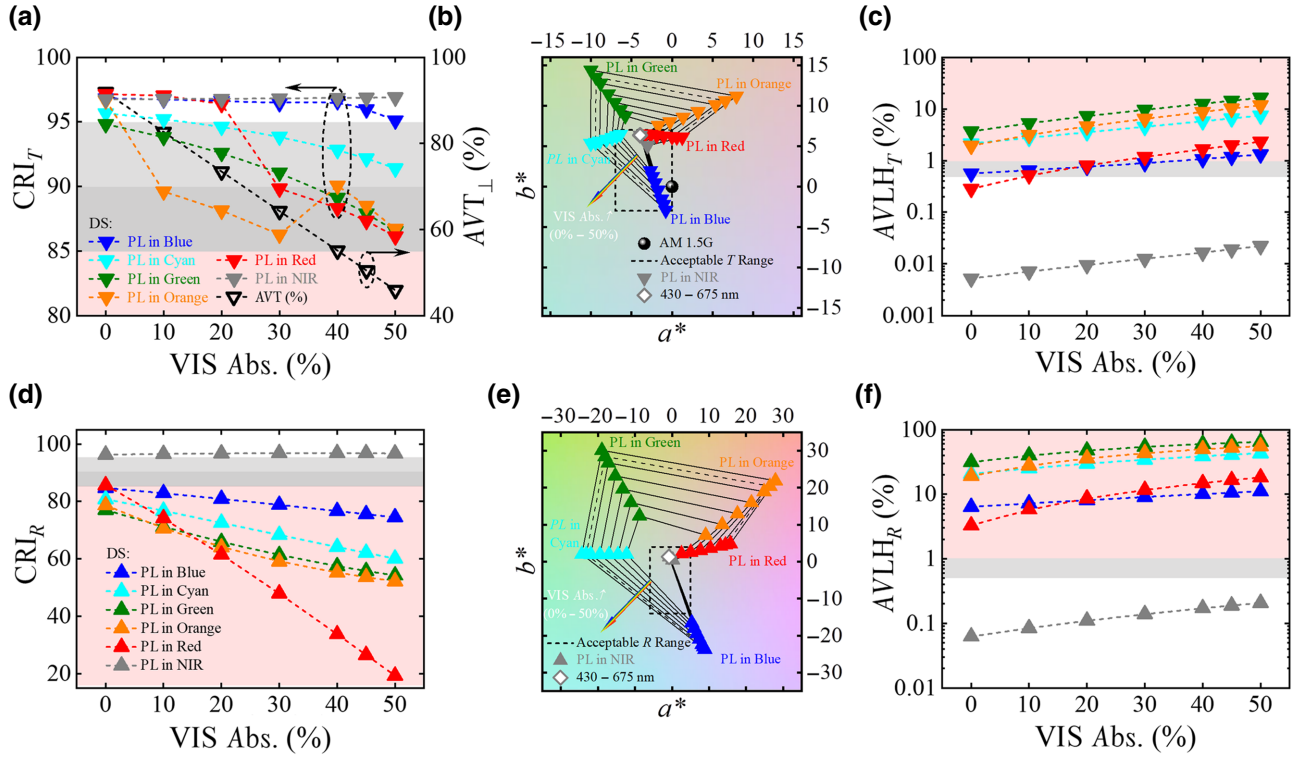

FIG. 4. The impact of escaped downshifting (DS) photoluminescence in different emission wavelengths on (a) CRI_T and $AVT_\perp$, (b) $(a^*, b^*)_T$, (c) average visible luminescent haze ($AVLH_T$), (d) CRI_R, (e) $(a^*, b^*)_R$, and (f) $AVLH_R$ as a function of degree of A_1. Note that different shades of background colors in (a) and (d) indicate various CRI grades of transparent window glasses on each side: 95–100 for "excellent" (in white), 90–95 for "good" (in light gray), 85–90 for "acceptable" (in dark gray), and below 85 for "poor" (in red). The dashed boxes in (b) and (e) indicate the acceptable (a^*, b^*) ranges: for $(a^*, b^*)_T$, $-7 < a^* < 0$ and $-3 < b^* < 7$; and for $(a^*, b^*)_R$, $-6 < a^* < 5$ and $-14 < b^* < 4$, which is based on the survey of many commercially available architectural glass products (see Supplemental Material Note 2 for detail [66]). The threshold value is 1% for AVLH on both sides; an AVLH range above 1% (in red) shade suggests strong visual impact from glowing haze due to escaped visible photoluminescence, which is unacceptable for window applications; an AVLH range between 0.5% and 1% (in gray) is less favorable for high-quality glazing systems. All the data shown in Fig. 4 are also tabulated in Supplemental Material Note 3 [66].

tinting out of the acceptable ranges on each side. On the transmitted side, we see that the aesthetics is outside the acceptable window for every emission color except those with PL(λ) in the blue for $A_1 < 50\%$, and PL(λ) in the red for $A_1 < 40\%$. On the reflected side, only LSCs with PL(λ) in the red and $A_1 < 10\%$ fall within the acceptable range.

Conventionally, the threshold value for scattering haze is limited to below 1% for high-quality architectural window glass (haze over 0.5%–1% creates an uncomfortable "cloudiness" for observers and therefore becomes unacceptable for high-quality glazing systems). The impact of glowing haze caused by escaped photoluminescence is also assessed, and the resulting $AVLH_T$s and $AVLH_R$s are plotted in logarithmic scale in Figs. 4(c) and 4(f), respectively. For all the PL colors, the $AVLH_T$s and $AVLH_R$s monotonically increase as more visible photons are harvested and contribute to the DS PL. The threshold requirement of 1% is also set for both $AVLH_T$ and $AVLH_R$ of LSCs with DS mechanisms as shown in Figs. 4(c) and 4(f), respectively. On the transmitted side, photoluminescence in cyan, green, and orange can cause strong glowing haze even with no VIS contribution, and photoluminescence in blue and red is acceptable with very limited VIS contribution between below 20% and 30%. On the reflected side, all visible photoluminescence results in corresponding $AVLH_R$ values over 1% regardless of the VIS contribution.

Figure 5 summarizes the aesthetic parameters of LSCs with TTA-UC and QC mechanisms as a function of PL(λ) peak wavelength. To isolate the impact from the TTA-UC and QC photoluminescence only, no VIS contribution is included in these assessments. As shown in Figs. 5(a) and 5(d), all upconverted emission in VIS range results in reduced CRI_Ts on the transmitted side. On the reflected side, the corresponding CRI_Rs are impacted even more strongly from the visible $PL^{Front}(\lambda)$, and all are unsuitable for window applications. Particularly, UC emission in the red results in CRI_R as low as 19.4. Accordingly, the (a^*, b^*) coordinates of the LSCs with visible UC emission are strongly tinted by the colors of the visible photoluminescence on both sides as shown in Figs. 5(b) and 5(e), and

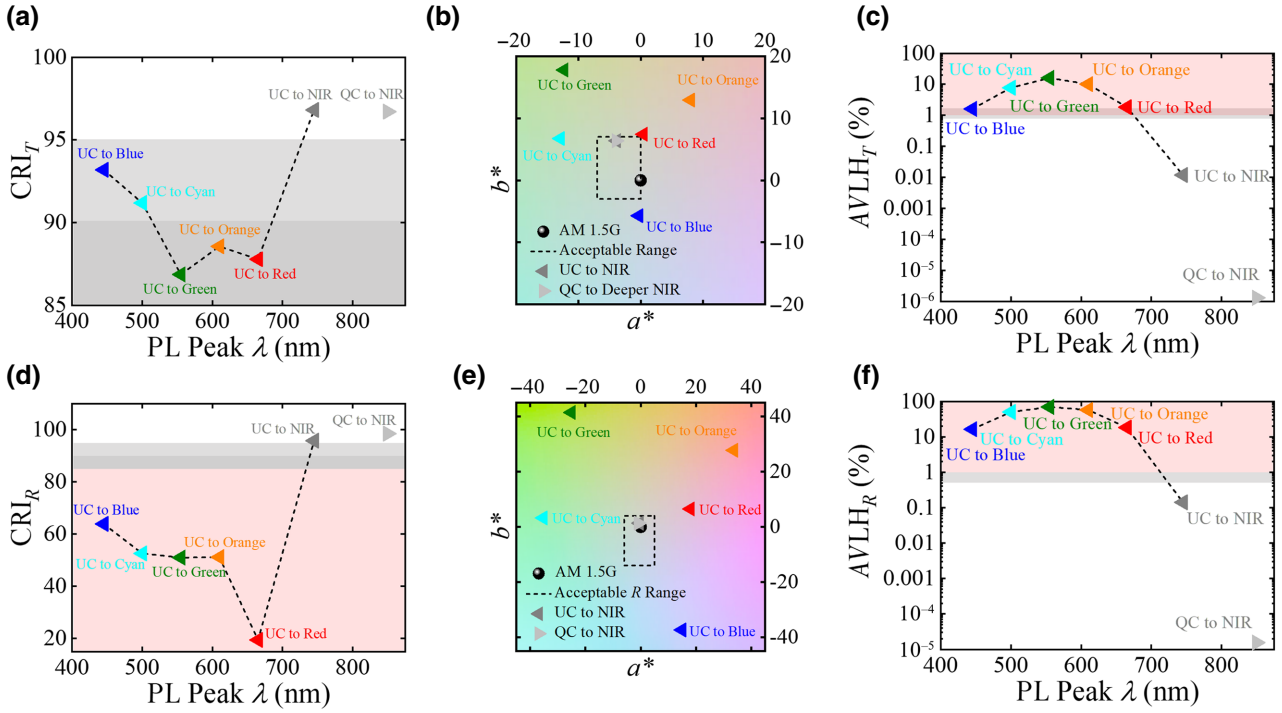

FIG. 5. The impact of escaped photoluminescence from upconversion (UC) and quantum cutting (QC) processes on (a) CRI_T, (b) $(a^*, b^*)_T$, (c) $AVLH_T$, (d) CRI_R, (e) $(a^*, b^*)_R$, and (f) $AVLH_R$ as a function of emission wavelength. All the data shown are also tabulated in Supplemental Material Note 3 [66].

all are outside of the acceptable range. Additionally, the "glowing" effect would be very prominent to observers on both sides of the LSCs with all the corresponding $AVLH_T$s and $AVLH_R$s well above the threshold value of 1%. In particular, $PL^{Front}(\lambda)$ in green results in $AVLH_R$ as high as 70% due to the close spectral match of $V(\lambda)$ and $PL(\lambda)$.

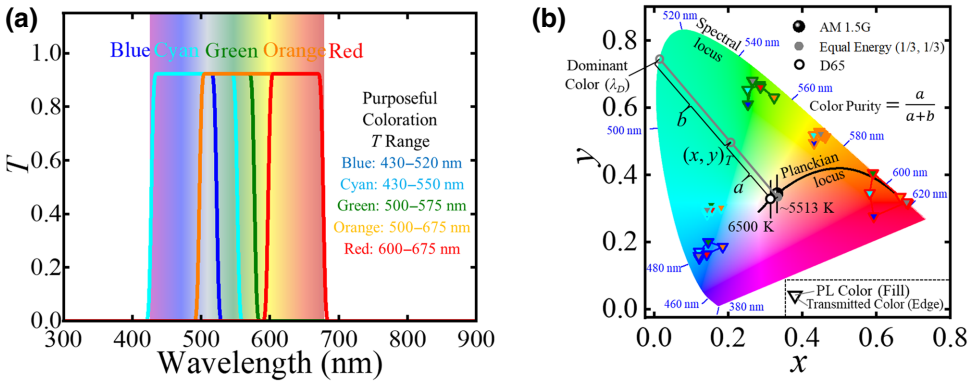

FIG. 6. (a) Idealized step-function transmittance profiles of LSCs with various purposeful coloration. (b) The impact of various escaped photoluminescence from DS process at different emission wavelengths on various transmitted colors. Note that the edge colors of the down-triangle legends represent the transmitted colors, and the fill colors of the triangle legends represent the photoluminescence colors. CIE 1931 color chromaticity diagrams are suitable to illustrate the high color purities of the transmitted colors under the impact of various escaped photoluminescence. As in the example shown in (b), the color purity (i.e., color saturation) of the transmitted color is the distance in the chromaticity diagram between a, the $(x, y)_T$ color coordinate point of the test source and the coordinate of the equal energy point of (1/3, 1/3), divided by $a+b$, the distance between the equal energy point and the dominant color wavelength point (x_d, y_d). Therefore, the color purity of $(x, y)_T$ is thus calculated as $\frac{a}{a+b} = \frac{\sqrt{(x-1/3)^2+(y-1/3)^2}}{\sqrt{(x_d-1/3)^2+(y_d-1/3)^2}}$. All the data shown in Fig. 6 are also tabulated in Supplemental Material Note 6 [66].

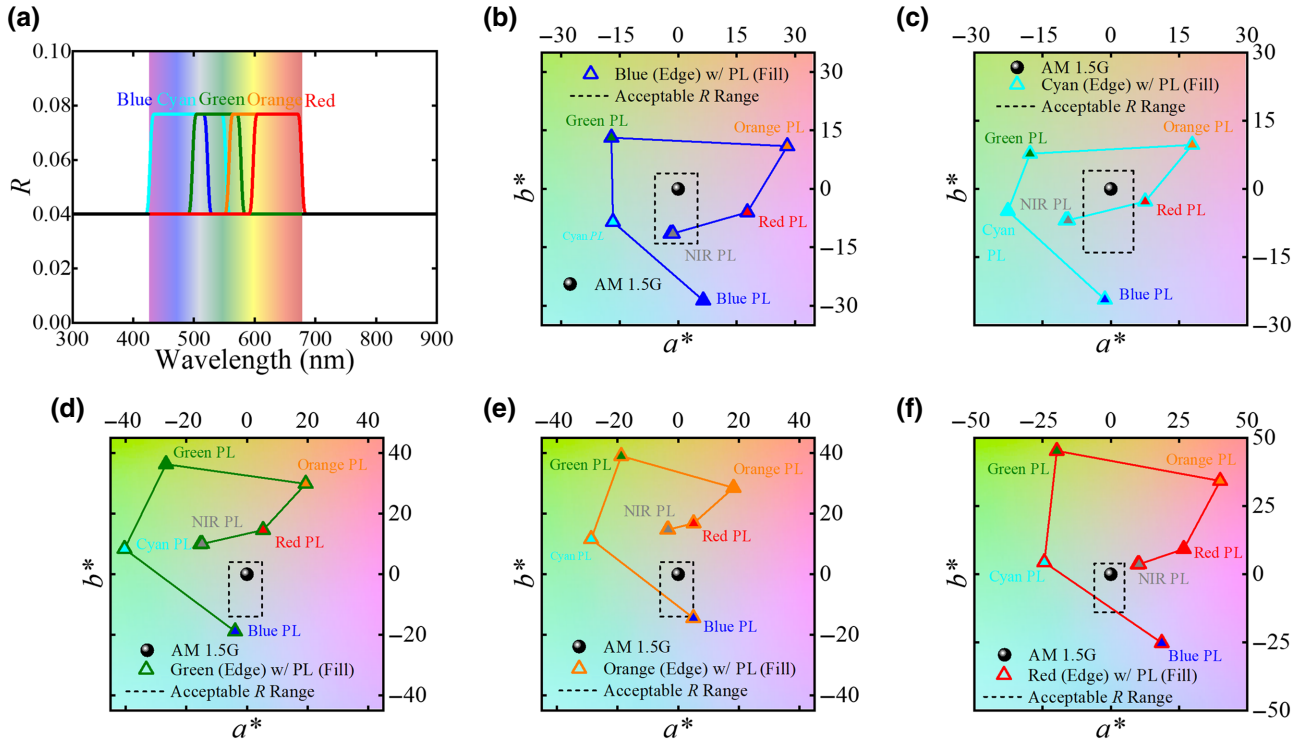

FIG. 7. (a) Idealized step-function reflected profiles of LSCs with various purposeful coloration. (b) The impact of various escaped photoluminescence from DS process in different emission wavelengths on (b) reflected blue color, (c) reflected cyan color, (d) reflected green color, (e) reflected orange color, and (f) reflected red color. Note that the edge colors of the up-triangle legends represent the reflected colors, and the fill colors of triangle legends represent the photoluminescence colors. All the data shown in Fig. 7 are also tabulated in Supplemental Material Note 6 [66].

B. Colorful applications

Absorption and emission peaks in VIS should be avoided in LSC designs where there is a preference for or requirement of color neutrality [1,5,16,17,20,23,25]. However, coloration can be desirable in particular LSC applications [57–59]. On the transmitted side as shown in Fig. 6, the transmitted photon fluxes [AM 1.5G(λ)·T(λ)] are strongly tinted in blue, cyan, green, orange, and red, respectively. As incident photons are harvested and down-shifted into visible photoluminescence, the escaped photoluminescence [PL^{Back}(λ)] exhibits impact on combined transmitted photon flux [AM 1.5G(λ)·T(λ) + PL^{Back}(λ)], shifting the $(x, y)_T$ coordinates of the transmitted colors and simultaneously impacting the corresponding color purities depending on the photoluminescence wavelength. Photoluminescence could thus reinforce, shift, or deteriorate transmissive or reflective color. Since the AM 1.5G(λ)·T(λ) is significantly stronger compared to the PL^{Back}(λ), the shift in $(x, y)_T$ is moderate as shown in Fig. 6(b), but the change in color purity can still be up to 0.2–0.25 (see Supplemental Material Note 6 for tabulated data [66]). The resulting $(x, y)_T$ coordinates of all the transmitted colors stay close to the spectral locus, suggesting relatively high color purities regardless of the impact of VIS photoluminescence colors. Although the transmitted color is dominated by the transmittance spectrum (i.e., the corresponding VIS absorption profile), the impact from the escaped photoluminescence is not negligible. On the other hand, the colors of reflected photon fluxes are less tinted, and the PL^{Front}(λ) fluxes are comparable to AM 1.5G(λ)·R(λ) fluxes, and as a result, the colors of PL^{Front}(λ) can substantially affect the overall colors of combined photon fluxes [AM 1.5G(λ)·R(λ) + PL^{Front}(λ)], driving the $(a^*, b^*)_R$ towards the corresponding colors of the visible photoluminescence as shown in Figs. 7(b)–7(f). Therefore, the impact from PL should similarly not be overlooked for these types of colorful LSCs.

V. DISCUSSION

A. Transparent applications

Significant effort and attention in LSC research have been focusing on improving luminophore QYs and suppressing reabsorption loss. However, it is also important to consider the various contributions to LSC aesthetics. As emitters are optimized and gradually approach theoretical limits for QY (100%, 50%, and 200% for DS, UC, and QC mechanisms, respectively) and absorption/harvesting

range, photoluminescence will continuously grow more impactful on all the key aspects of LSC aesthetics. This is particularly true when the PL(λ) is located in the VIS. In most cases, the impact on the (a^*, b^*) is unacceptable, and certainly so in nearly all cases when considering luminescent haze (as shown in Figs. 4 and 5). In contrast, the impact on CRI_T, CRI_R, $(a^*, b^*)_T$, and $(a^*, b^*)_R$ becomes negligible (even with high levels of visible contribution) as the DS photoluminescence is redshifted into NIR range. Additionally, glowing haze ($AVLH_T$ and $AVLH_R$) caused by NIR photoluminescence is also typically well below 0.5% (but depends on how much tail emission there is into the VIS). This effectively helps to maintain the high imaging fidelity and aesthetics on both sides. For DS photoluminescence, all incident photons with wavelengths shorter than the emission wavelengths can potentially contribute to the photovoltaic conversion, which results in the increasing peak height of the superimposed $PL^{Back}(\lambda)$ and $PL^{Front}(\lambda)$ as photoluminescence wavelength redshifts as shown in Fig. 3(c). With the same degree of $AVT_\perp$, LSCs with NIR photoluminescence not only minimize the visual impact, but also always maximize the utilization of the VIS contribution. Similarly, the UC process with NIR emission and the QC process deeper in the NIR can also effectively ensure that these LSC devices meet all aesthetic requirements for the highest demand window applications. As shown in Fig. 4, the corresponding CRIs exhibit the highest quality, the (a^*, b^*) coordinates reside very close to the origin, and the AVLHs are magnitudes below the threshold values on both sides of the LSC devices. Similarly to the DS process, as the PL(λ) redshifts, the usable solar spectrum for UC process also expands increasingly in the NIR and IR as shown in Fig. 3(f); for example, photons as deep as 1500 nm can potentially be utilized for the UC with NIR emission. In contrast, for UV-only selective harvesting TLSCs, the absorption cutoff is limited to below 430 nm to avoid yellow tints. The total photon flux at wavelengths below 430 nm is only about 3.7% of the AM 1.5G photon flux, therefore, the potential of these configurations seems limited. However, there are several strategies to effectively enhance the photovoltaic performance of UV-only TLSCs. First, the UV contribution can potentially be doubled by quantum cutting one high-energy UV photon into two NIR photons, where the corresponding NIR emission wavelengths typically match the peak external quantum efficiency of the commercially available edge-mounted PV, such as Si, GaAs, CIGS PVs, increasing the UV-only efficiency limits up to 5.6%. Such massive downshift across the VIS range is also advantageous for scaling to the practical size over 1 m [5,50–54]. Second, given a narrow emission profile and negligible overlapping with the UV absorption, the edge-mounted PV with large band gap (up to 2.88 eV) can be paired with a UV/blue emission profile (between about 435 and 440 nm) to minimize the voltage loss of the LSC-PV system, yielding a maximum PCE up to 6.9% [5]. In this UV-only selective configuration, the total energy flux at wavelengths below 430 nm is approximately 8.2% of the AM 1.5G energy flux (rather than photon flux), which ultimately determines the potential PCE limits [5,35,60,61]. Third, with optical isolation, the UV-only TLSC can be used as the top component and combined with other selective-harvesting LSC components to form multiband LSC-PV systems [6–8,17,62,63], which can simultaneously enhance the solar spectral coverage and protect other LSC components from high-energy photodegradation. It is important to note that some of these limitations can be partially mitigated by increasing the waveguide trapping efficiency (η_{Trap}). In theory, this can be improved to near 100% with combined antireflection coatings and distributed Bragg reflectors with tunable stop bands. In this case, the visual impact of photoluminescence would be effectively minimized or even eliminated for all photoluminescence mechanisms. However, such waveguiding enhancement can only be enabled when these optical designs are simultaneously applied onto both sides of the waveguide, and the stop bands need to spectrally match the PL (λ) wavelengths. If the PL(λ) and the corresponding stop bands reside within the VIS range (at normal or oblique incidence), the device will be strongly tinted from the corresponding $T(\lambda)$ and $R(\lambda)$ spectra as opposed to the PL spectra (a poor tradeoff), still exhibiting low color fidelity on both sides. While such an approach can potentially mitigate the impact of photoluminescence on the aesthetics, it comes at a substantial financial cost that would likely negate some or all of the low-cost advantage of an LSC approach. Similarly, the use of higher-refractive-index waveguides (i.e., glass) can simultaneously reduce waveguiding losses and photoluminescence impacting on the aesthetics, but also with the similar cost tradeoffs since high refractive index windows are not commonly/commercially available at large scales.

B. Colorful applications

In certain applications, surfaces with purposeful coloration are desired, and VIS luminescent haze can be incorporated to enhance such visual impact or expand the color tunability range. Herein, the VIS luminescence haze is deemed as a benefit rather than a detriment [64,65]. Figures 4(b), 4(e), 5(b), 5(e), 6(b), and 7(b)–7(f) show the expanded color tunability enabled by photoluminescence (in DS, UC, and QC) on the transmitted and reflected side, respectively. Notably, for LSCs with coloration from VIS absorption, if the AM $1.5G(\lambda)\cdot R(\lambda)$ and $PL^{Front}(\lambda)$ profiles are designed to overlap with each other, the preferred reflected colors can be further enhanced by the escaped VIS photoluminescence as shown in Figs. 7(b)–7(f). Furthermore, the combination of various coloration mechanisms (selective absorption, reflective coating, and VIS photoluminescence) offers diverse approaches to modify

the surface appearance (either the entire panel or partial surface coverage) instead of electrical power production; for example, the artistic potential of the LSCs can be exploited by utilizing different luminophores with various absorption and emission profiles as paints on transparent waveguides as canvases. Intricate patterns, special signage or even artistic creation can be applied, where luminescence can offer a unique visual perception or improved color saturation [57–59,64,65].

VI. CONCLUSIONS

Luminescent solar concentrators provide promising opportunities for widespread solar adoption due to their structural simplicity, ease of fabrication, design flexibility, and selective harvesting tunability. However, the significance of LSC aesthetics is often underestimated or ignored even though these metrics are often the key thresholds for practical applications. In this perspective, we first identify the key figures of merit for aesthetic quality of semitransparent and transparent LSC devices, and then we develop an optical model to quantitatively evaluate the rendered color fidelity and glowing haze of LSC systems by incorporating the impact of escaped photoluminescence. The aesthetics of LSCs with various photoluminescence mechanisms, including DS, UC, and QC processes, are systematically analyzed, and future strategies to simultaneously improve the photovoltaic performance and aesthetic quality of LSCs are proposed. For LSC applications with the requirements of minimum visual impact from escaped photoluminescence, the optimal approach is to shift the PL into NIR, which is also beneficial to minimize the overlap between absorption and emission profiles, suppressing the corresponding reabsorption loss. Quantitative analysis based on the optical model demonstrates the value of such an approach. As emitter materials with various photoluminescence mechanisms develop and the corresponding photoluminescence QYs improve, the consideration and optimization of the overall LSC photovoltaic performance and visual impact will start to emerge. Therefore, the goal of this work is to provide a roadmap for LSC development with aesthetic consideration in advance, so that the research can make LSC technologies more commercially appealing in both PV performance and aesthetic quality in the future. Purposeful coloration enabled by visible absorbing and emitting luminophores in LSC design is also quantitatively discussed. Visible photoluminescence could effectively reinforce, shift, or deteriorate the color rendering effects on both the transmitted and reflected sides of the LSCs. Ultimately, we expect this work can help guide researchers in developing comprehensive consideration of all the crucial aesthetic aspects in LSC design for a market-adoptable pathway.

ACKNOWLEDGMENTS

The authors gratefully acknowledge support from the National Science Foundation under Grant No. CBET-1702591 and the James Dyson Fellowship.

M.C.B. and R.R.L. are cofounders of Ubiquitous Energy Inc., a company working to commercialize transparent photovoltaic technologies. R.R.L. is a cofounder of GlowShop LLC, working to commercialize luminescent solar concentrator painting kits. All other authors declare no competing financial interest.

APPENDIX A: RELATIONSHIP BETWEEN IDEALIZED ABSORPTANCE, TRANSMITTANCE, AND REFLECTANCE FOR SINGLE-PANE MODULE

When the single-pane see-through PV is illuminated by incident solar irradiance, the light beam experiences multiple reflection and transmission events at the two air-PV interfaces. As shown in Fig. 8, the sum of the total reflected intensity and total transmitted intensity determines the total reflectance (R) and transmittance (T) of the see-through PV device, respectively. Here we derive the relationship between overall absorptance (A), transmittance, and reflectance for a single-pane module where the absorbing material is uniformly dispersed throughout the waveguide media.

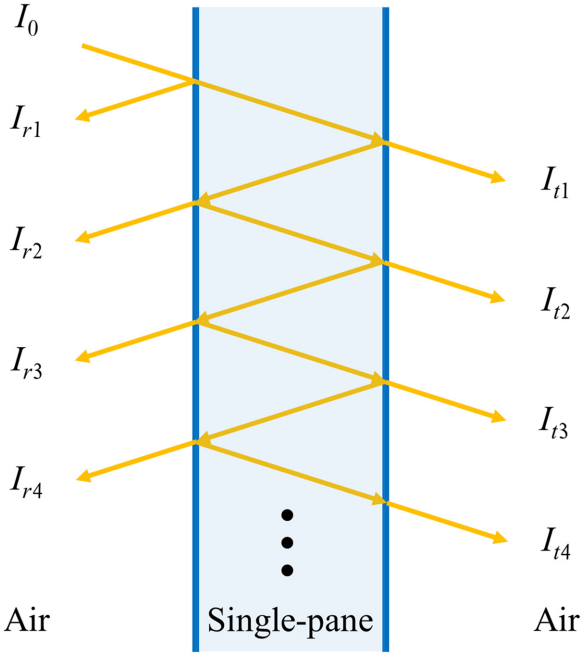

FIG. 8. Schematic showing that the incident light beam (I_0) experiences multiple reflection and transmission events when it interacts with a single-pane see-through PV device.

With refractive index, $n = 1.5$ of the see-through PV, the reflectance at the air-front surface interface (R_f) is

$$R_f = \left(\frac{n-1}{n+1}\right)^2 = 0.04.$$

According to the Beer-Lamber law, when an incident light beam transmits through a uniform attenuating medium with absorptivity (α), the single-pass transmittance (T_1) with an optical path length of d can be expressed as the ratio of the transmitted light beam intensity (I_t) to the incident light beam intensity (I_0):

$$T_1 = \frac{I_t}{I_0} = \exp(-\alpha \cdot d).$$

Therefore, the single-pass absorptance starting from within the media (A_1) is

$$A_1 = 1 - T_1 = 1 - \exp(-\alpha \cdot d).$$

For a single-pane see-through PV with multiple reflection and transmission events, the light beam intensity of each reflection and transmission event can be expressed as follows:
first order,

$$\begin{aligned} I_{r1} &= I_0 \cdot R_f, \\ I_{a1} &= I_0 \cdot (1 - R_f) \cdot A_1, \\ I_{t1} &= I_0 \cdot (1 - R_f) \cdot (1 - A_1) \cdot (1 - R_f) \\ &= I_0 \cdot (1 - R_f)^2 \cdot (1 - A_1); \end{aligned}$$

second order,

$$\begin{aligned} I_{r2} &= I_0 \cdot (1 - R_f) \cdot (1 - A_1) \cdot R_f \cdot (1 - A_1) \cdot (1 - R_f) \\ &= I_0 \cdot R_f \cdot (1 - R_f)^2 \cdot (1 - A_1)^2, \\ I_{a2} &= I_0 \cdot (1 - R_f) \cdot (1 - A_1) \cdot R_f \cdot A_1 + I_0 \cdot (1 - R_f) \cdot (1 - A_1) \cdot R_f \cdot (1 - A_1) \cdot R_f \cdot A_1 \\ &= I_0 \cdot (1 - R_f) \cdot A_1 \cdot [R_f \cdot (1 - A_1)] + I_0 \cdot (1 - R_f) \cdot A_1 \cdot [R_f \cdot (1 - A_1)]^2, \\ I_{t2} &= I_0 \cdot (1 - R_f) \cdot (1 - A_1) \cdot R_f \cdot (1 - A_1) \cdot R_f \cdot (1 - A_1) \cdot (1 - R_f) \\ &= I_0 \cdot (1 - R_f)^2 \cdot {R_f}^2 \cdot (1 - A_1)^3 = I_{t1} \cdot {R_f}^2 \cdot (1 - A_1)^2; \end{aligned}$$

third order,

$$\begin{aligned} I_{r3} &= I_0 \cdot (1 - R_f) \cdot (1 - A_1) \cdot R_f \cdot (1 - A_1) \cdot R_f \cdot (1 - A_1) \cdot R_f \cdot (1 - A_1) \cdot (1 - R_f) \\ &= I_0 \cdot (1 - R_f)^2 \cdot {R_f}^3 \cdot (1 - A_1)^4 = I_{r2} \cdot {R_f}^2 \cdot (1 - A_1)^2, \\ I_{a3} &= I_0 \cdot (1 - R_f) \cdot (1 - A_1) \cdot R_f \cdot (1 - A_1) \cdot R_f \cdot (1 - A_1) \cdot R_f \cdot A_1 \\ &\quad + I_0 \cdot (1 - R_f) \cdot (1 - A_1) \cdot R_f \cdot (1 - A_1) \cdot R_f \cdot (1 - A_1) \cdot R_f \cdot (1 - A_1) \cdot R_f \cdot A_1 \\ &= I_0 \cdot (1 - R_f) \cdot A_1 \cdot [R_f \cdot (1 - A_1)]^3 + I_0 \cdot (1 - R_f) \cdot A_1 \cdot [R_f \cdot (1 - A_1)]^4, \\ I_{t3} &= I_0 \cdot (1 - R_f) \cdot (1 - A_1) \cdot R_f \cdot (1 - A_1) \cdot R_f \cdot (1 - A_1) \cdot R_f \cdot (1 - A_1) \cdot R_f \cdot (1 - A_1) \cdot (1 - R_f) \\ &= I_0 \cdot (1 - R_f)^2 \cdot {R_f}^4 \cdot (1 - A_1)^5 = I_{t2} \cdot {R_f}^2 \cdot (1 - A_1)^2; \end{aligned}$$

fourth order,

$$\begin{aligned} I_{r4} &= I_0 \cdot (1 - R_f) \cdot (1 - A_1) \cdot R_f \cdot (1 - A_1) \cdot R_f \cdot (1 - A_1) \cdot R_f \cdot (1 - A_1) \cdot R_f \cdot (1 - A_1) \cdot R_f \cdot (1 - A_1) \cdot (1 - R_f) \\ &= I_0 \cdot (1 - R_f)^2 \cdot {R_f}^5 \cdot (1 - A_1)^6 = I_{r3} \cdot {R_f}^2 \cdot (1 - A_1)^2, \\ I_{a4} &= I_0 \cdot (1 - R_f) \cdot (1 - A_1) \cdot R_f \cdot (1 - A_1) \cdot R_f \cdot (1 - A_1) \cdot R_f \cdot (1 - A_1) \cdot R_f \cdot (1 - A_1) \cdot R_f \cdot A_1 \\ &\quad + I_0 \cdot (1 - R_f) \cdot (1 - A_1) \cdot R_f \cdot (1 - A_1) \cdot R_f \cdot (1 - A_1) \cdot R_f \cdot (1 - A_1) \cdot R_f \cdot (1 - A_1) \cdot R_f \cdot A_1 \\ &= I_0 \cdot (1 - R_f) \cdot A_1 \cdot [R_f \cdot (1 - A_1)]^5 + I_0 \cdot (1 - R_f) \cdot A_1 \cdot [R_f \cdot (1 - A_1)]^6, \\ I_{t4} &= I_0 \cdot (1 - R_f) \cdot (1 - A_1) \cdot R_f \cdot (1 - A_1) \cdot R_f \cdot (1 - A_1) \cdot R_f \cdot (1 - A_1) \cdot R_f \cdot (1 - A_1) \cdot R_f \cdot (1 - A_1) \\ &\quad \cdot R_f \cdot (1 - A_1) \cdot (1 - R_f) \\ &= I_0 \cdot (1 - R_f)^2 \cdot {R_f}^6 \cdot (1 - A_1)^7 = I_{t3} \cdot {R_f}^2 \cdot (1 - A_1)^2; \end{aligned}$$

...
*n*th order,

$$I_{rn} = I_{rn-1} \cdot {R_f}^2 \cdot (1 - A_1)^2,$$

$$I_{tn} = I_{tn-1} \cdot {R_f}^2 \cdot (1 - A_1)^2.$$

Both I_r and I_t are geometric sequences with common ratio of ${R_f}^2 \cdot (1 - A_1)^2 < 1$. It is noted that the R geometric sequence starts from the second order. The total reflectance and transmittance as the sum of the geometric sequences can therefore be calculated:

$$\sum_{i=1}^{\infty} I_{ri} = I_0 \cdot R_f + I_0 \cdot R_f \cdot (1 - R_f)^2 \cdot (1 - A_1)^2 + I_0 \cdot R_f \cdot (1 - R_f)^2 \cdot (1 - A_1)^2 \cdot [{R_f}^2 \cdot (1 - A_1)^2]$$
$$+ I_0 \cdot R_f \cdot (1 - R_f)^2 \cdot (1 - A_1)^2 \cdot [{R_f}^2 \cdot (1 - A_1)^2]^2 + I_0 \cdot R_f \cdot (1 - R_f)^2 \cdot (1 - A_1)^2 \cdot [{R_f}^2 \cdot (1 - A_1)^2]^3 + \ldots,$$

$$R = \frac{\sum_{i=1}^{\infty} I_{ri}}{I_0} = R_f + \frac{R_f \cdot (1 - R_f)^2 \cdot (1 - A_1)^2}{1 - {R_f}^2 \cdot (1 - A_1)^2}.$$

Similarly,

$$\sum_{i=1}^{\infty} I_{ti} = I_0 \cdot (1 - R_f)^2 \cdot (1 - A_1) + I_0 \cdot (1 - R_f)^2 \cdot (1 - A_1) \cdot [{R_f}^2 \cdot (1 - A_1)^2] + I_0 \cdot (1 - R_f)^2 \cdot (1 - A_1)$$
$$\cdot [{R_f}^2 \cdot (1 - A_1)^2]^2 + I_0 \cdot (1 - R_f)^2 \cdot (1 - A_1) \cdot [{R_f}^2 \cdot (1 - A_1)^2]^3 + \ldots,$$

$$T = \frac{\sum_{i=1}^{\infty} I_{ti}}{I_0} = \frac{(1 - R_f)^2 \cdot (1 - A_1)}{1 - {R_f}^2 \cdot (1 - A_1)^2}.$$

I_a is also a geometric sequence with a different common ratio of $R_f \cdot (1 - A_1)$, and the total absorptance can be calculated as

$$\sum_{i=1}^{\infty} I_{ai} = I_0 \cdot (1 - R_f) \cdot A_1 + I_0 \cdot (1 - R_f) \cdot A_1 \cdot [R_f \cdot (1 - A_1)] + I_0 \cdot (1 - R_f) \cdot A_1 \cdot [R_f \cdot (1 - A_1)]^2$$
$$+ I_0 \cdot (1 - R_f) \cdot A_1 \cdot [R_f \cdot (1 - A_1)]^3 + I_0 \cdot (1 - R_f) \cdot A_1 \cdot [R_f \cdot (1 - A_1)]^4$$
$$+ I_0 \cdot (1 - R_f) \cdot A_1 \cdot [R_f \cdot (1 - A_1)]^5 + I_0 \cdot (1 - R_f) \cdot A_1 \cdot [R_f \cdot (1 - A_1)]^6 + \ldots,$$

$$A = \frac{\sum_{i=1}^{\infty} I_{ai}}{I_0} = \frac{(1 - R_f) \cdot A_1}{1 - R_f \cdot (1 - A_1)}.$$

To confirm $A + T + R = 1$, the consistency derivation is shown below:

$$A + T + R = \left[\frac{(1 - R_f) \cdot A_1}{1 - R_f \cdot (1 - A_1)}\right] + \left[\frac{(1 - R_f)^2 \cdot (1 - A_1)}{1 - {R_f}^2 \cdot (1 - A_1)^2}\right] + \left[R_f + \frac{R_f \cdot (1 - R_f)^2 \cdot (1 - A_1)^2}{1 - {R_f}^2 \cdot (1 - A_1)^2}\right]$$
$$= \frac{(1 - R_f) \cdot A_1 \cdot [1 + R_f \cdot (1 - A_1)] + (1 - R_f)^2 \cdot (1 - A_1) + R_f \cdot (1 - R_f)^2 \cdot (1 - A_1)^2}{1 - {R_f}^2 \cdot (1 - A_1)^2} + R_f$$
$$= \frac{(1 - R_f) \cdot A_1 \cdot [1 + R_f \cdot (1 - A_1)] + (1 - R_f)^2 \cdot (1 - A_1) \cdot [1 + R_f \cdot (1 - A_1)]}{1 - {R_f}^2 \cdot (1 - A_1)^2} + R_f$$
$$= \frac{(1 - R_f) \cdot [1 + R_f \cdot (1 - A_1)] \cdot [A_1 + (1 - R_f) \cdot (1 - A_1)]}{1 - {R_f}^2 \cdot (1 - A_1)^2} + R_f$$
$$= \frac{(1 - R_f) \cdot [1 + R_f \cdot (1 - A_1)] \cdot [A_1 + 1 - R_f - A_1 + R_f \cdot A_1]}{1 - {R_f}^2 \cdot (1 - A_1)^2} + R_f$$

$$= \frac{(1-R_f)\cdot[1+R_f\cdot(1-A_1)]\cdot[1-R_f+R_f\cdot A_1]}{1-{R_f}^2\cdot(1-A_1)^2} + R_f$$
$$= \frac{(1-R_f)\cdot[1+R_f\cdot(1-A_1)]\cdot[1-R_f\cdot(1-A_1)]}{1-{R_f}^2\cdot(1-A_1)^2} + R_f$$
$$= \frac{(1-R_f)\cdot[1-{R_f}^2\cdot(1-A_1)^2]+R_f\cdot[1-{R_f}^2\cdot(1-A_1)^2]}{1-{R_f}^2\cdot(1-A_1)^2}$$
$$= \frac{(1-R_f+R_f)\cdot[1-{R_f}^2\cdot(1-A_1)^2]}{1-{R_f}^2\cdot(1-A_1)^2}$$
$$= \frac{1-{R_f}^2\cdot(1-A_1)^2}{1-{R_f}^2\cdot(1-A_1)^2} = 1.$$

In our optical model, different A_1 values in the visible range (430–675 nm) are input (e.g., $A_1 = 0, 0.1, 0.2, \ldots$) to create various idealized step-function absorptance profiles (A) as shown in Fig. 3(a): for example, with $A_1 = 0.2$ in the visible range, the calculated values are $R = 0.064$, $T = 0.738$, and $A = 0.198$; and with $A_1 = 1$ outside of visible range (below 430 nm and above 675 nm) we have $R = 0.04$, $T = 0$, and $A = 0.96$.

APPENDIX B: AVERAGE VISIBLE LUMINESCENT HAZE DEFINITION

In an LSC system with simple waveguide and isotropic emitters as shown in Fig. 9, the incident light beam is transmitted and reflected only in the normal direction, which determines the corresponding $\mathrm{AVT}_\perp$ and the average visible reflectance ($\mathrm{AVR}_\perp$), respectively. On the other hand, the untrapped photoluminescence escapes from both sides of the waveguide in all directions, which determines the corresponding AVLH_T and AVLH_R.

In the window and plastics industries, the scattering haze is defined as the ratio of the transmitted light that is scattered to the total transmitted light (the sum of specular transmittance and diffusive transmittance) [43,44]. The definition of scattering haze is therefore referenced to quantify the glowing haze. On the transmitted side:

$$\mathrm{AVT}_\perp = \frac{\int \mathrm{AM\ 1.5G}(\lambda)\cdot T(\lambda)\cdot V(\lambda)d\lambda}{\int \mathrm{AM\ 1.5G}(\lambda)\cdot V(\lambda)d\lambda},$$
$$\mathrm{AVT}_{\mathrm{Glowing}} = \frac{\int \mathrm{PL}^{\mathrm{Back}}(\lambda)\cdot V(\lambda)d\lambda}{\int \mathrm{AM\ 1.5}G(\lambda)\cdot V(\lambda)d\lambda},$$

where $T(\lambda)$ is the transmittance spectrum directly measured by the double-beam spectrometer (with no blank sample on the reference side) and $\mathrm{PL}^{\mathrm{Back}}(\lambda)$ is the absolute escaped photoluminescence photon flux on the transmitted (back) side of the waveguide that is a function of the waveguide trapping efficiency (η_{Trap}) and the absolute total photoluminescence photon flux [$\mathrm{PL}^{\mathrm{Total}}(\lambda)$] as

$$\mathrm{PL}^{\mathrm{Back}}(\lambda) = 0.5\times(1-\eta_{\mathrm{Trap}})\cdot\mathrm{PL}^{\mathrm{Total}}(\lambda) = 0.5 \times\left(1-\sqrt{1-1/{n_{\mathrm{Sub}}}^2}\right)\cdot\mathrm{PL}^{\mathrm{Total}}(\lambda).$$

The factor of 0.5 accounts for each side, and the product $0.5\times\left(1-\sqrt{1-1/{n_{\mathrm{Sub}}}^2}\right)$ is approximately 12.7%. The corresponding AVLH_T is then defined based on the traditional definition of haze as the fraction of diffuse component to the sum of specular and diffusive components:

$$\mathrm{AVLH}_T = \frac{\mathrm{AVT}_{\mathrm{Glowing}}}{\mathrm{AVT}_\perp + \mathrm{AVT}_{\mathrm{Glowing}}}.$$

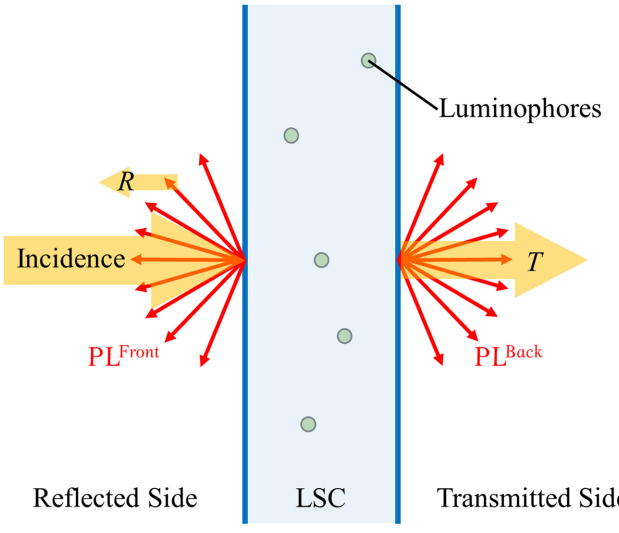

FIG. 9. Schematic showing the transmitted and reflected light (orange arrows) and the escaped photoluminescence (red arrows).

Similarly, on the reflected side,

$$\mathrm{AVR}_{\perp} = \frac{\int \mathrm{AM\ 1.5G}(\lambda)\cdot R(\lambda)\cdot V(\lambda)d\lambda}{\int \mathrm{AM\ 1.5G}(\lambda)\cdot V(\lambda)d\lambda},$$

$$\mathrm{AVR}_{\mathrm{Glowing}} = \frac{\int \mathrm{PL}^{\mathrm{Front}}(\lambda)\cdot V(\lambda)d\lambda}{\int \mathrm{AM\ 1.5G}(\lambda)\cdot V(\lambda)d\lambda} = \mathrm{AVT}_{\mathrm{Glowing}},$$

where, $R(\lambda)$ is the reflectance spectrum, which can also be directly measured by the double-beam spectrometer. Then the corresponding AVLH_R is defined as

$$\mathrm{AVLH}_R = \frac{\mathrm{AVR}_{\mathrm{Glowing}}}{\mathrm{AVR}_{\perp} + \mathrm{AVR}_{\mathrm{Glowing}}}.$$

[1] C. J. Traverse, R. Pandey, M. C. Barr, and R. R. Lunt, Emergence of highly transparent photovoltaics for distributed applications, Nat. Energy **2**, 849 (2017).

[2] O. Almora, *et al.*, Device performance of emerging photovoltaic materials (version 1), Adv. Energy Mater. **11**, 2002774 (2021).

[3] A. Goetzberger and W. Greube, Solar energy conversion with fluorescent collectors, Appl. Phys. **14**, 123 (1977).

[4] M. G. Debije and P. P. C. Verbunt, Thirty years of luminescent solar concentrator research: Solar energy for the built environment, Adv. Energy Mater. **2**, 12 (2012).

[5] C. Yang and R. R. Lunt, Limits of visibly transparent luminescent solar concentrators, Adv. Opt. Mater. **5**, 1600851 (2017).

[6] K. Wu, H. Li, and V. I. Klimov, Tandem luminescent solar concentrators based on engineered quantum dots, Nat. Photonics **12**, 105 (2018).

[7] H. Zhao, D. Benetti, X. Tong, H. Zhang, Y. Zhou, G. Liu, D. Ma, S. Sun, Z. M. Wang, Y. Wang, and F. Rosei, Efficient and stable tandem luminescent solar concentrators based on carbon dots and perovskite quantum dots, Nano Energy **50**, 756 (2018).

[8] F. Mateen, M. Ali, S. Y. Lee, S. H. Jeong, M. J. Ko, and S.-K. Hong, Tandem structured luminescent solar concentrator based on inorganic carbon quantum dots and organic dyes, Sol. Energy **190**, 488 (2019).

[9] N. D. Bronstein, Y. Yao, L. Xu, E. O'Brien, A. S. Powers, V. E. Ferry, A. P. Alivisatos, and R. G. Nuzzo, Quantum dot luminescent concentrator cavity exhibiting 30-fold concentration, ACS Photonics **2**, 1576 (2015).

[10] M. R. Bergren, N. S. Makarov, K. Ramasamy, A. Jackson, R. Guglielmetti, and H. McDaniel, High-performance $CuInS_2$ quantum dot laminated glass luminescent solar concentrators for windows, ACS Energy Lett. **3**, 520 (2018).

[11] H. Li, K. Wu, J. Lim, H.-J. Song, and V. I. Klimov, Doctor-blade deposition of quantum dots onto standard window glass for Low-loss large-area luminescent solar concentrators, Nat. Energy **1**, 16157 (2016).

[12] F. Meinardi, H. McDaniel, F. Carulli, A. Colombo, K. A. Velizhanin, N. S. Makarov, R. Simonutti, V. I. Klimov, and S. Brovelli, Highly efficient large-area colourless luminescent solar concentrators using heavy-metal-free colloidal quantum dots, Nat. Nanotechnol. **10**, 878 (2015).

[13] F. Meinardi, S. Ehrenberg, L. Dhamo, F. Carulli, M. Mauri, F. Bruni, R. Simonutti, U. Kortshagen, and S. Brovelli, Highly efficient luminescent solar concentrators based on earth-abundant indirect-bandgap silicon quantum dots, Nat. Photonics **11**, 177 (2017).

[14] F. Meinardi, A. Colombo, K. A. Velizhanin, R. Simonutti, M. Lorenzon, L. Beverina, R. Viswanatha, V. I. Klimov, and S. Brovelli, Large-Area luminescent solar concentrators based on Stokes-shift-engineered' nanocrystals in a mass-polymerized PMMA matrix, Nat Photonics **8**, 392 (2014).

[15] H.-Y. Huang, K.-B. Cai, P.-W. Chen, C.-A. J. Lin, S.-H. Chang, and C.-T. Yuan, Engineering ligand–metal charge transfer states in cross-linked gold nanoclusters for greener luminescent solar concentrators with solid-state quantum yields exceeding 50% and low reabsorption losses, J. Phys. Chem. C **122**, 20019 (2018).

[16] Y. Zhao and R. R. Lunt, Transparent luminescent solar concentrators for large-area solar windows enabled by massive stokes-shift nanocluster phosphors, Adv. Energy Mater. **3**, 1143 (2013).

[17] C. Yang, W. Sheng, M. Moemeni, M. Bates, C. K. Herrera, B. Borhan, and R. R. Lunt, Ultraviolet and near-infrared dual-band selective-harvesting transparent luminescent solar concentrators, Adv. Energy Mater. **n/a**, 2003581 (2021).

[18] A. Sanguineti, A. Monguzzi, G. Vaccaro, F. Meinardi, E. Ronchi, M. Moret, U. Cosentino, G. Moro, R. Simonutti, M. Mauri, R. Tubino, and L. Beverina, NIR emitting ytterbium chelates for colourless luminescent solar concentrators, Phys. Chem. Chem. Phys. **14**, 6452 (2012).

[19] T. Wang, J. Zhang, W. Ma, Y. Luo, L. Wang, Z. Hu, W. Wu, X. Wang, G. Zou, and Q. Zhang, Luminescent solar concentrator employing rare earth complex with zero self-absorption loss, Sol. Energy **85**, 2571 (2011).

[20] C. Yang, J. Zhang, W. T. Peng, W. Sheng, D. Liu, P. S. Kuttipillai, M. Young, M. R. Donahue, B. G. Levine, B. Borhan, and R. R. Lunt, Impact of stokes shift on the performance of near-infrared harvesting transparent luminescent solar concentrators, Sci. Rep. **8**, 16359 (2018).

[21] M. G. Debije, P. P. C. Verbunt, P. J. Nadkarni, S. Velate, K. Bhaumik, S. Nedumbamana, B. C. Rowan, B. S. Richards, and T. L. Hoeks, Promising fluorescent dye for solar energy conversion based on a perylene perinone, Appl. Opt. **50**, 163 (2011).

[22] M. J. Currie, J. K. Mapel, T. D. Heidel, S. Goffri, and M. A. Baldo, High-Efficiency organic solar concentrators for photovoltaics, Science **321**, 226 (2008).

[23] C. Yang, M. Moemeni, M. Bates, W. Sheng, B. Borhan, and R. R. Lunt, High-performance near-infrared harvesting transparent luminescent solar concentrators, Adv. Opt. Mater. **8**, 1901536 (2020).

[24] C. Yang, D. Liu, and R. R. Lunt, How to accurately report transparent luminescent solar concentrators, Joule **3**, 2871 (2019).

[25] C. Yang, D. Liu, A. Renny, P. S. Kuttipillai, and R. R. Lunt, Integration of near-infrared harvesting transparent luminescent solar concentrators onto arbitrary surfaces, J. Lumin. **210**, 239 (2019).

[26] J. C. Goldschmidt and S. Fischer, Upconversion for photovoltaics – a review of materials, devices and concepts

for performance enhancement, Adv. Opt. Mater. **3**, 510 (2015).
[27] S.-J. Ha, J.-H. Kang, D. H. Choi, S. K. Nam, E. Reichmanis, and J. H. Moon, Upconversion-assisted dual-band luminescent solar concentrator coupled for high power conversion efficiency photovoltaic systems, ACS Photonics **5**, 3621 (2018).
[28] H. C. Bauser, C. R. Bukowsky, M. Phelan, W. Weigand, D. R. Needell, Z. C. Holman, and H. A. Atwater, Photonic crystal waveguides for >90% light trapping efficiency in luminescent solar concentrators, ACS Photonics **7**, 2122 (2020).
[29] J. L. Banal, B. Zhang, D. J. Jones, K. P. Ghiggino, and W. W. H. Wong, Emissive molecular aggregates and energy migration in luminescent solar concentrators, Acc. Chem. Res. **50**, 49 (2017).
[30] J. L. Banal, H. Soleimaninejad, F. M. Jradi, M. Liu, J. M. White, A. W. Blakers, M. W. Cooper, D. J. Jones, K. P. Ghiggino, S. R. Marder, T. A. Smith, and W. W. H. Wong, Energy migration in organic solar concentrators with a molecularly insulated perylene diimide, J. Phys. Chem. C **120**, 12952 (2016).
[31] J. L. Banal, J. M. White, K. P. Ghiggino, and W. W. H. Wong, Concentrating aggregation-induced fluorescence in planar waveguides: A proof-of-principle, Sci. Rep. **4**, 4635 (2014).
[32] Y. Zhou, D. Benetti, Z. Fan, H. Zhao, D. Ma, A. O. Govorov, A. Vomiero, and F. Rosei, Near infrared, highly efficient luminescent solar concentrators, Adv. Energy Mater. **6**, 1501913 (2016).
[33] I. Coropceanu and M. Bawendi, Core/shell quantum dot based luminescent solar concentrators with reduced reabsorption and enhanced efficiency, Nano Lett. **14**, 4097 (2014).
[34] N. C. Giebink, G. P. Wiederrecht, and M. R. Wasielewski, Resonance-shifting to circumvent reabsorption loss in luminescent solar concentrators, Nat. Photonics **5**, 694 (2011).
[35] D. Liu, C. Yang, and R. R. Lunt, Halide perovskites for selective ultraviolet-harvesting transparent photovoltaics, Joule **2**, 1827 (2018).
[36] R. R. Lunt, Theoretical limits for visibly transparent photovoltaics, Appl. Phys. Lett. **101**, 43902 (2012).
[37] C. Yang, D. Liu, M. Bates, M. C. Barr, and R. R. Lunt, How to accurately report transparent solar cells, Joule **3**, 1803 (2019).
[38] C. Yang, *et al.*, Consensus statement: Standardized reporting of power-producing luminescent solar concentrator performance, Joule **6**, 8 (2022).
[39] Z. Li, T. Ma, H. Yang, L. Lu, and R. Wang, Transparent and colored solar photovoltaics for building integration, Sol. RRL **5**, 2000614 (2021).
[40] H. J. Snaith, How should you measure your excitonic solar cells?, Energy Environ. Sci. **5**, 6513 (2012).
[41] E. Zimmermann, P. Ehrenreich, T. Pfadler, J. A. Dorman, J. Weickert, and L. Schmidt-Mende, Erroneous efficiency reports harm organic solar cell research, Nat. Photonics **8**, 669 (2014).
[42] M. G. Debije, P. P. C. Verbunt, B. C. Rowan, B. S. Richards, and T. L. Hoeks, Measured surface loss from luminescent solar concentrator waveguides, Appl. Opt. **47**, 6763 (2008).
[43] ASTM D1003 - 13.
[44] ISO 14782:1999.
[45] J. de Wild, A. Meijerink, J. K. Rath, W. G. J. H. M. van Sark, and R. E. I. Schropp, Upconverter solar cells: Materials and applications, Energy Environ. Sci. **4**, 4835 (2011).
[46] M. J. Y. Tayebjee, D. R. McCamey, and T. W. Schmidt, Beyond Shockley–Queisser: Molecular approaches to high-efficiency photovoltaics, J. Phys. Chem. Lett. **6**, 2367 (2015).
[47] X. Jiang, X. Guo, J. Peng, D. Zhao, and Y. Ma, Triplet–triplet annihilation photon upconversion in polymer thin film: Sensitizer design, ACS Appl. Mater. Interfaces **8**, 11441 (2016).
[48] S. Wen, J. Zhou, P. J. Schuck, Y. D. Suh, T. W. Schmidt, and D. Jin, Future and challenges for hybrid upconversion nanosystems, Nat. Photonics **13**, 828 (2019).
[49] C. Ye, V. Gray, J. Mårtensson, and K. Börjesson, Annihilation versus excimer formation by the triplet pair in triplet–triplet annihilation photon upconversion, J. Am. Chem. Soc. **141**, 9578 (2019).
[50] D. M. Kroupa, J. Y. Roh, T. J. Milstein, S. E. Creutz, and D. R. Gamelin, Quantum-cutting ytterbium-doped $CsPb(Cl_{1-x}Br_x)_3$ perovskite thin films with photoluminescence quantum yields over 190%, ACS Energy Lett. **3**, 2390 (2018).
[51] T. A. Cohen, T. J. Milstein, D. M. Kroupa, J. D. MacKenzie, C. K. Luscombe, and D. R. Gamelin, Quantum-cutting Yb^{3+}-doped perovskite nanocrystals for monolithic bilayer luminescent solar concentrators, J. Mater. Chem. A **7**, 9279 (2019).
[52] T. J. Milstein, D. M. Kroupa, and D. R. Gamelin, Picosecond quantum cutting generates photoluminescence quantum yields over 100% in ytterbium-doped $CsPbCl_3$ nanocrystals, Nano Lett. **18**, 3792 (2018).
[53] T. Cai, J. Wang, W. Li, K. Hills-Kimball, H. Yang, Y. Nagaoka, Y. Yuan, R. Zia, and O. Chen, Mn^{2+}/Yb^{3+} codoped $CsPbCl_3$ perovskite nanocrystals with triple-wavelength emission for luminescent solar concentrators, Adv. Sci. **7**, 2001317 (2020).
[54] D. Zhou, D. Liu, G. Pan, X. Chen, D. Li, W. Xu, X. Bai, and H. Song, Cerium and ytterbium codoped halide perovskite quantum dots: A novel and efficient downconverter for improving the performance of silicon solar cells, Adv. Mater. **29**, 1704149 (2017).
[55] C. Yang and R. R. Lunt, Comment on "upconversion-assisted dual-band luminescent solar concentrator coupled for high power conversion efficiency photovoltaic systems,", ACS Photonics **8**, 678 (2021).
[56] K. Kim, S. K. Nam, J. Cho, and J. H. Moon, Photon upconversion-assisted dual-band luminescence solar concentrators coupled with perovskite solar cells for highly efficient semi-transparent photovoltaic systems, Nanoscale **12**, 12426 (2020).
[57] A. Reinders, R. Kishore, L. Slooff, and W. Eggink, Luminescent solar concentrator photovoltaic designs, Jpn. J. Appl. Phys. **57**, 08RD10 (2018).
[58] J. ter Schiphorst, M. L. M. K. H. Y. K. Cheng, M. van der Heijden, R. L. Hageman, E. L. Bugg, T. J. L. Wagenaar, and M. G. Debije, Printed luminescent solar concentrators: Artistic renewable energy, Energy Build. **207**, 109625 (2020).

[59] F. M. Vossen, M. P. J. Aarts, and M. G. Debije, Visual performance of red luminescent solar concentrating windows in an office environment, Energy Build. **113**, 123 (2016).

[60] D. Chen, Y. Ba, M. Deng, W. Zhu, W. Chai, H. Xi, D. Chen, J. Zhang, C. Zhang, and Y. Hao, High-purity, thick $CsPbCl_3$ films toward selective ultraviolet-harvesting visibly transparent photovoltaics, ACS Appl. Energy Mater. **4**, 12121 (2021).

[61] D. Liu, C. Yang, P. Chen, M. Bates, S. Han, P. Askeland, and R. R. Lunt, Lead halide ultraviolet-harvesting transparent photovoltaics with an efficiency exceeding 1%, ACS Appl. Energy Mater. **2**, 3972 (2019).

[62] L. Zdražil, S. Kalytchuk, K. Holá, M. Petr, O. Zmeškal, Š Kment, A. L. Rogach, and R. Zbořil, A carbon dot-based tandem luminescent solar concentrator, Nanoscale **12**, 6664 (2020).

[63] C. Liu and B. Li, Multiple dyes containing luminescent solar concentrators with enhanced absorption and efficiency, J. Opt. **17**, 25901 (2015).

[64] M. Kanellis, M. M. de Jong, L. Slooff, and M. G. Debije, The solar noise barrier project: 1. Effect of incident light orientation on the performance of a large-scale luminescent solar concentrator noise barrier, Renewable Energy **103**, 647 (2017).

[65] M. G. Debije, R. C. Evans, and G. Griffini, Laboratory protocols for measuring and reporting the performance of luminescent solar concentrators, Energy Environ. Sci. **14**, 293 (2021).

[66] See Supplemental Material at http://link.aps.org/supplemental/10.1103/PhysRevApplied.17.034054 for the survey of mass-market glass product statistics, tabulated data, and idealized spectral profiles of LSCs with purposeful coloration.